

Characterization of fracture void space heterogeneity by electrical impedance measurement

A. Boschan^{a,b,c}, I. Ippolito^{b,c}, R. Chertcoff^{b,c}, J. P. Hulin^{a,c}, H. Auradou^{a,c}

^a*Univ Pierre et Marie Curie-Paris 6, Univ Paris-Sud, CNRS, Lab. FAST, Bâtiment 502, Campus Paris-Sud, Orsay, F – 91405 France*

^b*Grupo de Medios Porosos, Departamento de Física, Facultad de Ingeniería, Universidad de Buenos Aires, Paseo Colón 850, 1063 Buenos Aires, Argentina.*

^c*LIA PMF-FMF (Franco-Argentinian International Associated Laboratory in the Physics and Mechanics of Fluids)*

Abstract

The possible characterization of the heterogeneity of the aperture field in rough fractures by electrical impedance measurement is demonstrated through displacement experiments using two miscible fluids of different electrical resistivity. Two model fractures have been used: their complementary rough walls are identical but have different relative shear displacements creating “channel” or “barrier” structures in the void space, respectively parallel or perpendicular to the mean flow velocity \vec{U} . In the (“channel”) geometry, the global electrical resistance displays an initial linear variation followed by a “tail” part reflecting the contrast between slow and fast flow channels. In the (“barrier”) geometry, the existence of a change in the slope between two linear zones suggests the appearance of domains of different permeabilities along the fracture. These variations are well reproduced theoretically and numerically either by assuming independent flow channels parallel to \vec{U} (channel case) or an aperture that varies only along the flow (barrier case). For each configuration, we present a specific inversion procedure that allows one to extract the key features of the heterogeneity from the resistance variation.

Keywords: fractures, solute, heterogeneity, channeling, electrical, roughness

1. Introduction

Many important industrial processes such as nuclear or chemical waste storage or water management involve fractured media (NAS, 1996; Neretnieks et al., 1982; Neretnieks, 2002). While the characteristics of fracture networks is an important question, modelling them requires a good knowledge of their individual elements. Single fractures have often been represented as the space between two parallel-plate surfaces: however, numerous studies revealed that their flow and transport properties are strongly influenced by the roughness of the walls and the spatial variations of their local aperture (Oron and Berkowitz, 1998; Keller et al., 1999; Meheust and Schmittbuhl, 2000; Matsuki et al., 2006; Watanabe et al., 2008; Nemoto et al., 2009). The determination of the geometrical and transport properties of individual fractures is therefore a key

issue in view of practical applications: their heterogeneity may, for instance, lead to the appearance of channeling effects.

Even though elaborate laboratory techniques have been developed to characterize the heterogeneity of porous media, few methods allow one to characterize in-situ a single fracture. In the present paper, we demonstrate experimentally at the lab scale that electrical impedance measurements may provide such information while being adaptable to field configurations.

In a pioneering work, Brown (Brown, 1989) showed that the electrical impedance of a fracture saturated by a conducting fluid depends on the geometrical organization of the void space. The electrical aperture of fractures with fractal wall surfaces was shown to be lower than that for parallel plane walls of comparable size and distance: this results from the increased tortuosity of the iso potential lines.

At the scale of a fracture network, Odling et al. (2007) demonstrated that impedance measurements may be used to determine the effective dispersion coefficient of a small network of fractures created in a granite plug. After saturating completely the sample by a fluid of known conductivity, they injected a second fluid of different conductivity and measured the variations of the impedance of the fracture network with time during the displacement. The longitudinal dispersion coefficient and the hydrodynamic retardation coefficient were then derived from these variations: their values were shown to depend both on the connectivity of the network and on the spatial distribution and density of the fractures.

Our objective is here to apply a similar measurement method to single rough fractures. In this latter case, previous studies performed by means of other experimental techniques have demonstrated that tracer dispersion is largely determined by the spatial organization of the free space between the fracture walls. Neretnieks et al. (1982) analyzed the motion and spreading of a tracer carried by a fluid flow inside a single natural fissure in a granitic sample: they observed a non Fickian dispersion even for non sorbing tracers. This behavior was accounted for by preferential channelling within the fracture plane. Bauguet and Fourar (2008) investigated experimentally the different case of model fractures with heterogeneities stratified in the direction perpendicular to the mean flow.

A relative shear displacement of the fracture walls was recently found to be one of the mechanisms leading to the localization of the flow in preferential paths, particularly for complementary rough walls with a self-affine geometry (Yeo et al., 1998; Auradou et al., 2005; Nemoto et al., 2009). In this latter case, the mean effective hydraulic aperture depends on the relative orientation of the flow and the shear: it increases for a flow perpendicular to the shear and decreases when it is parallel to it. A statistical analysis of the aperture field demonstrated that these features are due to structural heterogeneities preferentially perpendicular to the shear. In a fracture of similar geometry saturated by a stagnant conducting solution, electrical measurements in a radial current configuration demonstrated a variation of the electrical resistance with the orientation of the relative displacement (Plouraboue et al., 2000).

More recently, Boschan et al. (2009) used a light transmission technique and transparent rough fracture models to measure dispersion for flow either parallel or normal to the shear. The features of the dispersion process are very different in the two cases. When flow is normal to the structures created by the shear, the Fickian description is

valid and tracer spreading is characterized by a single dispersion coefficient: this case is referred to in the following as the “barrier” geometry. When flow is parallel to the structures induced by the shear, these act as preferential channels, leading to the appearance of fingers and to a non Fickian dispersion: this case will be referred to as the “channel” geometry.

In the present study, the same transparent models as in the previous work of Boschan et al. (2009) are used to monitor the variations of the global electrical impedance of the fracture during displacement experiments using saline tracers. This allows one to determine relative concentration maps from the light transmission images simultaneously with the electrical measurements. Also, the aperture field of this fracture may be determined by comparing images corresponding to a full saturation by the two pure fluids.

After describing the fracture models and the experimental procedure, electrical resistance measurements performed during displacement at different Péclet numbers in the “channel” and “barrier” geometries are reported. We discuss qualitatively these observations, and then compare with quantitative theoretical predictions in the simple case of parallel plates; then, two different simple descriptions of the void space for the “channel” and “barrier” geometries are presented. The analytical and numerical predictions in these two configurations are significantly different and are compared to the corresponding experimental results. Finally, the inversion of the resistance data in order to estimate the aperture distributions is discussed: different approaches are needed for the barrier and channel geometries.

2. Experimental setup and procedure

The realization of the transparent rough fracture models and the optical technique for performing dispersion measurements are described in detail by Boschan et al. (2009).

2.1. Fracture models

The roughness of the fracture walls is obtained by carving plexiglas blocks by means of a computer controlled milling machine from a self-affine surface map (1360×360 points): the corresponding value of Hurst’s exponent is $\zeta = 0.8$ like for a broad range of materials (see Poon et al. (1992); Bouchaud (2003)). The length of the models is $L = 350$ mm and their width $w = 90$ mm (the length L is parallel to the mean flow which corresponds to the axis x). The geometries of the two walls are complementary; they match perfectly when brought in contact and are identical for the two experimental. A normal displacement (equal to the mean aperture) is then introduced from this contact position together with a relative shear displacement $\vec{\delta}$ of magnitude $|\vec{\delta}| = 0.75$ mm, parallel to the length L for one of the models and perpendicular for the other. In both cases, the mean value of the local aperture $a(x, y)$ is $\langle a(x, y) \rangle_{x,y} = 0.75$ mm and its standard deviation $\sigma_a = 0.14$ mm.

Grey level maps of these aperture fields are displayed in Figs. 1 and 2. As can be observed, the shear displacement $\vec{\delta}$ introduces “heterogeneity structures” always normal to $\vec{\delta}$ (*i.e.* to y in the first case and to x in the second): the correlation length of the aperture is larger parallel than perpendicular to them.

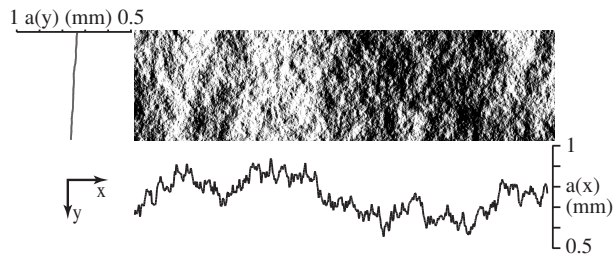


Figure 1: Top right: grey level map of the numerical aperture field in the “barrier geometry”: white = 1 mm, black = 0.5 mm. Map size: 1360 by 360 pixels. Bottom: profile of the average $a(x) = \langle a(x, y) \rangle_y$ of the aperture over the width w of the model; left: profile of the average $a(y) = \langle a(x, y) \rangle_x$ over the length L .

When the structures are normal to the mean flow (*i.e.* to x , they may act as barriers (Fig.2): one refers therefore to this case as the “barrier” geometry. Then, the average $a(x) = \langle a(x, y) \rangle_y$ of the aperture in the y direction (bottom curve in Fig. 2) displays large variations with x ; in contrast, the variations of $a(y) = \langle a(x, y) \rangle_x$ with y are much smaller (curve at the left).

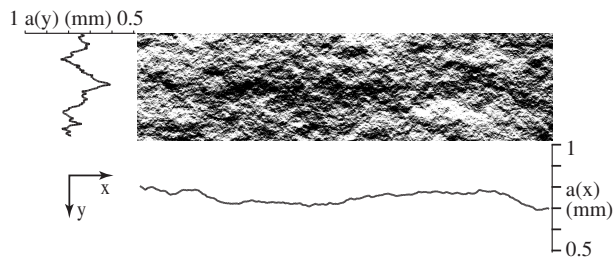


Figure 2: Top right - Grey level map of the numerical aperture in the “channel geometry”: The size of the map, the grey level code and the meaning of the curves at the bottom and at the left are the same as in Fig. 1.

When the heterogeneity structures are dominantly parallel to the mean flow (and, therefore, to x), they may act as preferential channels (Fig.1): for this reason, this case is referred to in the following as the “channel” geometry. In the map of Fig. 1, there is, for instance, a zone of low aperture half way between the lateral sides of the model and extending along most of its length. These “channels” produce large variations with y of the average $a(x) = \langle a(x, y) \rangle_x$ of the aperture (left curve) while $a(y) = \langle a(x, y) \rangle_y$ varies much less with x (bottom curve).

2.2. Experimental set up and fluids

Figure 3 displays the experimental setup used for the dispersion measurements. The fracture model is positioned with its length vertical. The corresponding sides (acting as lateral borders) are sealed while the two horizontal sides are open. The upper side of the model is connected to a syringe pump sucking the fluids upward out of the fracture. The lower horizontal side is dipped into a fluid bath which may be moved up and down: this allows one to replace the fluids conveniently in the initial phase of the

experiments. The fracture model is transparent and placed between a light panel and a Roper Coolsnap HQ video camera.

For electrical measurements, two stainless steel grids ($90 \times 20 \times 1 \text{ mm}^3$) used as the electrodes are placed in the fluid bath and in the outlet, and connected to a HP 4284A impedance analyzer with a measurement frequency of 1 kHz.

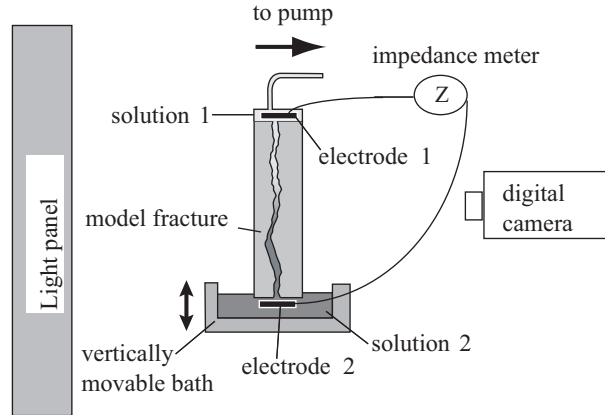


Figure 3: Schematic view of the fracture model.

The fluids used here are Non-Newtonian shear thinning solutions with the same concentration of scleroglucan (1000 ppm) in water. Their rheological characteristics are discussed by Boschan et al. (2009). One fluid is dyed with 0.3 g/l of Anilin Blue dye (*Handbook of dyes* (2002)) while the other contains the same amount of NaCl (as a result, the first fluid is dark blue and the second transparent). This allows one to minimize buoyancy driven instabilities by matching the densities of the two fluids and also to introduce a contrast between their electrical conductivities and light transmissivities. For clarity and concision, the two solutions are referred to in the following as d (dye) and s (salt). Their respective electrical conductivities are $\sigma_s = 2.27 \text{ mS/cm}$ and $\sigma_d = 2 \text{ mS/cm}$.

Polymer solutions have been selected in these experiments for two reasons. First, at high velocities, their shear thinning properties enhance the macrodispersion due to large scale heterogeneities of the flow field (Boschan et al., 2009): this macrodispersion is reflected by large structures of the displacement front which provide valuable information on the heterogeneities. Moreover, at low flow velocities, the effective viscosity of the solutions is high: this further reduces the development of unwanted buoyancy driven instabilities due to residual density contrasts.

2.3. Experimental procedure for displacement experiments

The fracture is first saturated by one of the solutions s or d ; then, the fluid bath is moved down, emptied, cleaned, filled with the other fluid, and moved up until the model is again in contact with the fluid of the bath. Finally, the experiment is initiated by pumping fluid at the top of the model at a constant flow rate: the mean fluid velocity

U ranges between 0.0024 and 0.24 mm/s (or $2.8 < Pe < 285$ in which the Péclet number Pe is defined by $Pe = U \langle a(x, y) \rangle_{x,y} / D_m$). This procedure allows one to obtain a very flat horizontal displacement front at the initial time. During the experiments, both light transmission and electrical impedance measurements are performed at a constant rate. The time variation of the real (resistance) and the imaginary (reactance) components of the impedance are recorded.

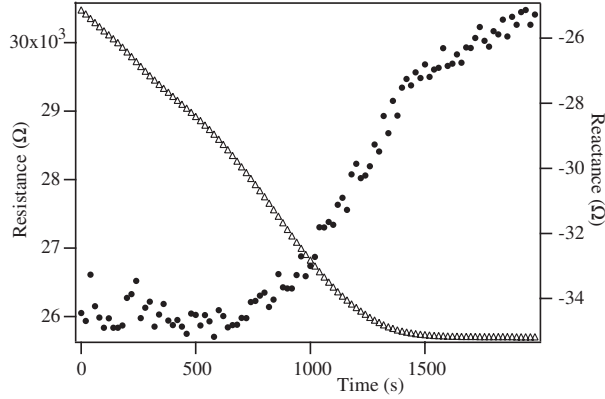


Figure 4: Variation of the resistance (Δ) and reactance (\bullet) of a rough model fracture as a function of time during the displacement solution d by solution s of lower electrical resistivity .

Figure 4 displays a typical variation of the resistance and reactance as a function of time when solution d is replaced by solution s . In this case, the resistance decreases monotonously from a value corresponding to the more resistive fluid down to a lower one corresponding to a full saturation of the model by the least resistive solution.

The variation of the reactance is more than two orders of magnitude smaller than that of the resistance so that the curve is much noisier; moreover, its physical meaning is not obvious. The rest of the paper deals therefore exclusively with resistance variations.

The electrical conductivity of the plexiglas is negligible compared to that of the fluid conductivity and no absorption of the ions on the fracture surface was detected. The measured resistance corresponds to that of the fluid saturating the slit between the two walls (the contribution of the resistance of the inlet and outlet which have a far larger aperture is much lower).

Fig. 4 also shows that the variation of the resistance during the experiment is globally roughly linear between initial and final limiting values: it is shown below that important information on the flow structure resides in deviations from this linear variation.

2.4. Resistance measurements for pure solutions.

Before analyzing the time variation during a displacement process of the resistance of the two fractures, we discuss first their values when they are fully saturated by either solutions s or d . The objective is to investigate the influence of the conductivity of the fluids and to compare the values obtained for the two fractures with a same fluid. The

values of the real part of the electrical impedance measured for the two models and the two solutions s and d are listed in Table 1.

	R_s (k Ω)	R_d (k Ω)	R_s/R_d	R/R^{pp}
Barrier	25.5 ± 0.2	30.5 ± 0.2	0.835 ± 0.01	1.15 ± 0.03
Channel	21.5 ± 0.2	26.5 ± 0.2	0.81 ± 0.01	0.98 ± 0.04

Table 1: R_s , R_d , R_s/R_d : values of the electrical resistance of the fracture models and ratio of these values when the models are fully saturated by solutions s or d . R/R^{pp} : ratio of the measured resistance and of that corresponding to the parallel plate model (averaged over solutions s and d).

In the range of measurement frequencies and voltages used in the present work, the electrical resistance is expected to be proportional to the resistivity of the saturating fluid. Under these assumptions, the ratio R_s/R_d of the resistivities measured for fluids s and d should be the same for the two models: the values of these ratios listed in Table 1 are indeed equal to within $\pm 2\%$ so that:

$$\frac{R_s}{R_d} = \frac{\rho_s}{\rho_d} = 0.82 \pm 0.02. \quad (1)$$

As a result, the ratio of the electrical resistances measured for the two models saturated by a same solution is also independent of the solution with:

$$\frac{R_{channel}}{R_{barrier}} = 0.85 \pm 0.03. \quad (2)$$

The values of the resistances have been compared to those predicted by the parallel plate assumption for an effective aperture a equal to the average $\langle a(x, y) \rangle_{x,y} = 0.75$ mm (identical for the two models). The corresponding resistances are respectively $R_s^{pp} = L/(w a \sigma_s) = 22.8$ k Ω and $R_d^{pp} = L/(w a \sigma_d) = 26$ k Ω .

The values of the ratio R/R^{pp} are listed in Table 1: it is close to one in the channel geometry and 10% higher in the barrier one. This implies that, in this latter case, the roughness has a stronger influence on the fracture resistance. The difference reflects the anisotropy of the aperture field: similar differences between two such configurations, of even larger amplitude, have been reported for the values of the permeability (Auradou et al., 2005).

These static measurements confirm the linear variation of the fluid resistance with the electrical resistivity of the fluid. This suggests to use a normalized variable in order to eliminate the influence of the values of σ_s and σ_d . The resistance R is then replaced by the normalized parameter R^* :

$$R^* = \frac{R - R_d}{R_s - R_d} \quad (3)$$

for flows where the dyed fluid displaces the salt solution and by

$$R^* = \frac{R - R_s}{R_d - R_s} \quad (4)$$

in the opposite situation (fluid s replacing fluid d). In this way, R^* is always equal to 1 at the beginning of the experiments and to 0 when the injected fluid has completely replaced the displaced one. In order to compare more easily experiments performed at different mean flow velocities U , the time t is also replaced by the reduced variable: $t^* = Ut/L$. Note that $t^* = 1$ corresponds to an injected volume equal to the pore volume of the fracture.

3. Displacement experiments: measurements results.

In this section we discuss the experimental variations of $R^*(t)$ as a function of the reduced time t^* in the channel and barrier geometry; values of the Péclet number ranging from 28 to 285 have been investigated.

In both figures 5 and 6, the data correspond to experiments in which fluid s displaces fluid d . Inverse experiments in which the dyed fluid displaces the $NaCl$ solutions have also been performed. The variations of $R^*(t^*)$ obtained in the two cases are the same: this demonstrates that no gravitational instabilities due to residual density contrasts appear and that the displacement is not influenced by other differences between the two solutions.

3.1. Channel geometry.

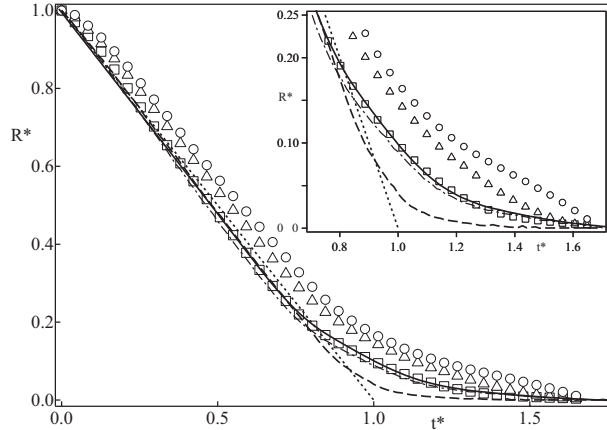


Figure 5: Variation of the normalized resistance R^* as a function of the reduced time t^* in the channel geometry. Experimental data for (\circ): $Pe = 28$, (\triangle): $Pe = 142$, (\square): $Pe = 285$. Dotted line: parallel plate model, solid (resp. dashed dotted) lines: predictions of analytical and numerical models from Sec. 4.2 for $n = 0.26$; dashed line: theoretical model for $n = 1$. Inset: enlarged view of bottom right of the main graph.

The resistance R^* decreases at first linearly with t^* with a constant slope up to $t^* \simeq 0.7$ (Fig. 5). For $t^* \geq 0.7$, one observes a tail-like variation and the slope decreases continuously to zero. R^* becomes zero only for values of t^* significantly larger than 1. This indicates that a sizable fraction of the displaced fluid is located in slow flow paths and leaves the model significantly after the mean transit time ($t^* = 1$) corresponding to

the injection of one pore volume. The variations of $R^*(t^*)$ with t^* at the different Péclet numbers are qualitatively similar: the slope at short times (and therefore the efficiency of the displacement) increases with Pe . At long times, the full displacement ($R^* = 0$) is obtained roughly at the same normalized time at all Pe values (*i.e.* $t^* \sim 1.5 - 1.7$).

3.2. Barrier geometry.

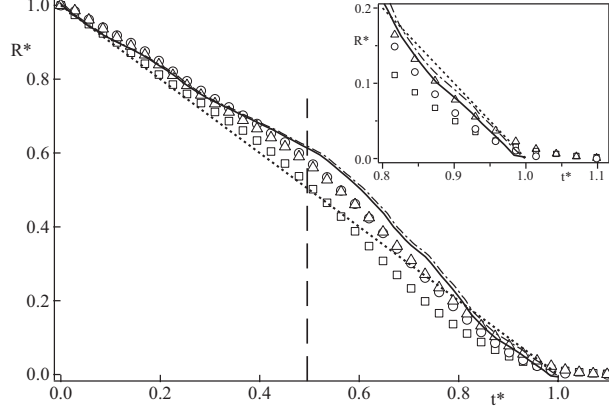


Figure 6: Variation of the normalized resistivity R^* (see Eqs. (3) and (4)) as a function of the reduced time t^* in the barrier geometry. The symbols used for the experimental data are the same as in Fig. 5. Dotted line: parallel plate model (Eq.(10)), solid (resp. dashed dotted) lines: predictions of analytical and numerical models from Sec. 4.3. Vertical dashed line: value of t^* at the transition between variations of $R^*(t^*)$ with different slopes. Inset: enlarged view of bottom right of the main graph.

Unlike the previous case (Fig. 5), the full saturation by the displacing fluid (*i.e.* $R^* = 0$) is nearly reached for $t^* = 1$ (injection of one pore volume) at all Péclet numbers and the tail-like features are barely visible (Fig. 6). This indicates that no continuous slow or fast flow paths are present in the model.

Moreover, unlike in the channel case, the slope dR^*/dt^* does not vary monotonously with time: it is lower than the average trend for $0 < t^* < 0.5$ and higher for $0.5 < t^* < 0.8$ (the transition is marked by the vertical dashed line in Fig. 6). Moreover, the variations of the slope with t^* are significantly larger at the two lowest Péclet numbers than for $Pe = 285$.

The observations in the channel and barrier geometries and the differences between them confirm therefore that, in both configurations, the variation of R^* with t^* provides information on the structure of the flow field.

4. Displacement experiments: models

In this section, the resistance variation curves are modeled first in the simplest case of a parallel plate approximation and then using two different simplified representations of the flow field for the parallel and perpendicular cases.

4.1. Parallel plates geometry.

The description assuming two parallel plane surfaces at a distance a provides a reference curve for determining the deviations induced by different kinds of heterogeneities of the flow field. Also, this assumption will be used to evaluate the influence of the conductivity contrast between the two solutions and of the mixing zone which develops between the two fluids after the flow is established.

Regarding this latter issue, at large enough times, the combination of advection and transverse molecular diffusion leads to a diffusive spreading regime often called Taylor dispersion (Taylor, 1953; Boschan et al., 2003). The average c_d of the concentration of fluid d over the aperture satisfies then :

$$c_d(\zeta) = \frac{1}{2}(1 \pm \text{Erf}(\zeta)); \quad (5)$$

where $\zeta = (x - Ut)/(2\sqrt{Dt})$, x is the distance from the fracture inlet, U the mean flow velocity, t the time and D the dispersion coefficient. In this equation, the plus (respectively minus) sign corresponds to the situation in which the fracture is initially saturated by the dyed (respectively transparent) fluid.

For flow between parallel plates, the local resistivity $\rho(x, y, t)$ is constant in the y direction, so that the overall electrical resistance is related to the variation along the length L of the fracture by:

$$R(t) = \frac{1}{aw} \int_0^L \rho(x, t) dx \quad (6)$$

in which $\rho(x, y, t) = \rho(x, t)$ is related to the local relative concentration c_d of dyed fluid by: $1/\rho(x, t) = c_d(x, t)\sigma_d + (1 - c_d(x, t))\sigma_s$. Eq. (6) then becomes:

$$R(t) = \frac{1}{\sigma_s aw} \int_0^L \frac{1}{1 - \chi c_d(x, t)} dx \quad (7)$$

where $\chi = 1 - \sigma_d/\sigma_s$. Due to the small contrast between the conductivities σ_s and σ_d ($\chi = 0.12$), one can assume that $\chi c_d \ll 1$: Eq. (7) may then be approximated by:

$$R(t) \simeq \frac{1}{\sigma_s aw} \left(L + \chi \int_0^L c_d(x, t) dx \right). \quad (8)$$

The integral at the right is the ratio of the volume of dyed fluid inside the fracture by the section aw transverse to the mean flow. For a fracture initially saturated by the salt solution, mass conservation requires that this integral be equal to Qt/aw in which Q is the volume flow rate. Then, Eq. (8) becomes:

$$R(t) \simeq \frac{1}{\sigma_s w} \left(\frac{L}{a} + \chi \frac{Q}{a^2 w} t \right). \quad (9)$$

Since the ratio $Q/(aw)$ is equal to the mean velocity U which is also that of the front, the resistance varies linearly from $R_s = L/(aw\sigma_s)$ to $R_d = L/(aw\sigma_d)$. In the other flow configuration (dyed fluid displaced by salt solution), Qt must be replaced by $awL - Qt$.

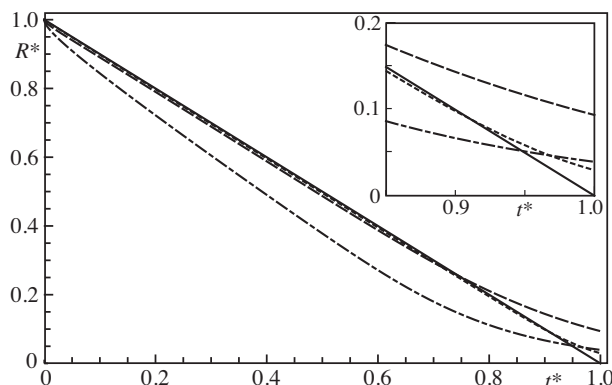


Figure 7: Variation of the resistance with time in the parallel plate model. Solid line: prediction from Eq. (10). Dotted and dashed lines: normalized resistivity variation $R^*(t^*)$ computed by integrating Eq. (7) for $\chi = 0.12$ and, respectively, $\alpha/a = 1$ and $\alpha/a = 10$. Dash-dotted line: variation of $R^*(t^*)$ computed for $\alpha/a = 10$ and $\chi = 0.7$. Inset: enlarged view of bottom right of the main graph.

Using the normalized variables R^* and t^* defined in Sec. 2.4, Eq. (9) becomes:

$$R^* = 1 - t^*. \quad (10)$$

This variation is represented by a straight dotted line as a reference in Figs. 5 and 6. Due to the normalization, the slope is always negative ($= -1$) while it may be of either sign for the variation of $R(t)$.

The variation from Eq. (10) does not depend on the dispersion coefficient D : this is however only valid as long as the upstream part of the concentration variation front has not reached the end of the fracture and all the injected fluid has remained within it.

In order to evaluate the influence of this latter effect, as well as of the approximation made by replacing Eq. (7) by Eq. (8), Eq. (7) has been integrated directly, using Eq. (5) in order to estimate $c_d(x, t)$. The dispersion coefficients D (or equivalently the normalized dispersivities $\alpha/a = D/(Ua)$) are taken equal to the upper and lower values determined previously from sequences of images of the displacement front (Boschan et al., 2009). The result of this computation is compared in Fig. 7 to the linear variation from Eq. (10).

For $\chi = 0.12$ (value used in the present experiments), the curves computed from Eq. (7) are, at first, only slightly below the linear variation from Eq. (10). When the forward part of the displacement front reaches the end of the model, there is an upward curvature of the variation and R^* becomes larger than the value predicted by the parallel plate model as $t^* \rightarrow 1$ (see inset). This occurs earlier for $\alpha/a = 10$ ($t^* \simeq 0.75$) than for $\alpha/a = 1$ ($t^* \simeq 0.92$): this difference reflects the broader width of the front due to dispersion for $\alpha/a = 10$. The value of R^* differs still significantly from 0 at $t^* = 1$: this shows that the saturation of the fracture by the displacing fluid is incomplete.

For the larger conductivity ratio $\chi = 0.7$, the curve derived from Eq. (7) (dash-dotted line) is clearly below the linear variation predicted by Eq. (10): this implies that the first order approximation used to obtain Eq. (8) is not valid any more. Even when

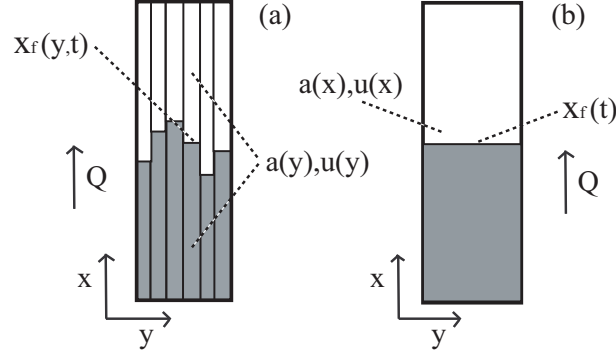


Figure 8: Schematic view of the front geometry with the aperture and velocity distributions for the channel (left) and barrier (right) models. Grey (white) zones: portions of the fracture saturated with the displacing (respectively displaced) fluid. For the channel model, discretized channels are shown for simplicity but the aperture $a(y)$ and the velocity $u(y)$ are actually continuous functions of y .

the deviation from the linear variation is large, none of the curves obtained for different values of α/a and χ displays abrupt slope variations comparable to those observed on the experimental curve of Fig. 6.

The above results demonstrate that the variation of the electrical resistance is mainly determined by the overall translation of the displacement front separating regions saturated by solutions of different electrical conductivities. The hydrodynamic dispersion only adds a tail feature to the curves for t^* values close to 1. In the following models, χ is always taken small and the variation of the resistance are assumed to be determined exclusively by convective processes (*i.e.* the effect of local dispersion is neglected).

We shall now take into account the effect of the heterogeneities of the flow field by means of two different models specifically adapted to either the perpendicular or the parallel case.

4.2. Channel geometry

Velocity field and front displacement. In this case, the fracture is described as a set of independent channels parallel to the mean flow (see Fig. 8a) and of aperture $a(y)$ constant with x : a previous study (Boschan et al., 2009), has indeed shown that this model reproduces well the large scale geometry of the displacement front (defined as the isoconcentration line $c = 0.5$). As in Fig. 1, $a(y)$ is equal to the average $\langle a(x, y) \rangle_x$.

In order to compute explicitly the profile of the front separating the two fluids, the polymer solutions used in the present experiments are assumed to be power law shear thinning fluids of rheological exponent n at the highest Péclet numbers (the effective viscosity μ is related to the shear rate $\dot{\gamma}$ by : $\mu \propto \dot{\gamma}^{-n}$). The value $n = 0.26$ has been obtained by means of independent rheological measurements (see Boschan et al. (2009)). The velocity $u(y)$ is then :

$$u(y) = \frac{\bar{u} a(y)^{(n+1)/n}}{\langle a(y)^{(n+1)/n} \rangle_y} \quad (11)$$

in which $\bar{u} = \langle u(y) \rangle_y$ is the mean fluid velocity across the fracture. The front profile $x_f(y, t)$ is then given by:

$$x_f(y, t) = u(y)t \quad (12)$$

The resulting profiles display large structures with an amplitude increasing linearly with time (Boschan et al., 2009).

A low Pe values (low velocities), the solutions behave like Newtonian fluids with $\mu = cst.$, corresponding to $n = 1$.

Analytical computation of the resistance. Since local dispersion is neglected, a local element of the fracture is assumed to be fully saturated by one of the pure fluids s or d : the displacement front is therefore the boundary between two regions occupied by each pure fluid.

In a first step, the variation with time of the effective resistance of the fracture is computed by assuming that, like for mass flow, there is no transverse transport of electrical current. Then, Eq. (7) is applied to each elementary channel by replacing a by its local value $a(y)$ and taking into account the variation of $c_d(c, y, t)$ with y . The elementary channels are in parallel so that their conductances add up. Using again a first order approximation with respect to $\chi \ll 1$ provides the following expression of the global effective conductance:

$$\frac{1}{R(t)} = \frac{\sigma_s}{L} \int_0^w a(y) \left(1 - \frac{\chi}{L} \int_0^L c_d(x, y, t) dx \right) dy. \quad (13)$$

For an elementary channel at a distance y , the integral of c_d with respect to x is either equal to L if the front has reached the end of the model ($u(y)t \geq L$) or to $u(y)t$ otherwise ($u(y)t \leq L$). Therefore:

$$\frac{1}{R(t)} = \frac{\sigma_s}{L} \int_{u(y)t \leq L} a(y) \left(1 - \frac{\chi}{L} u(y)t \right) dy + \frac{\sigma_s}{L} \int_{u(y)t \geq L} a(y) (1 - \chi) dy. \quad (14)$$

At early times such that $u(y)t \leq L$ for all y , $1/R$ varies linearly with t with:

$$\frac{1}{R(t)} = \frac{\sigma_s}{L} \int_0^w a(y) dy - \frac{\sigma_s \chi t}{L^2} \int_0^w a(y) u(y) dy \quad (15)$$

Again using a first order approximation for $\chi \ll 1$, Eq. (15) may be rewritten in the following form equivalent to Eq. (9):

$$R(t) = \frac{L}{\sigma_s \int_0^w a(y) dy} \left[1 + \frac{\chi t}{L} \frac{\int_0^w a(y) u(y) dy}{\int_0^w a(y) dy} \right] \quad (16)$$

This expression becomes identical to Eq. (10) for R^* defined from Eq. 3 and t^* taken equal to Ut/L (U is here the arithmetic mean $\int_0^L a(y) u(y) dy / \int_0^L a(y) dy$).

This initial linear regime is left for $t_1^* = U/U_M \leq 1$ in which u_M is the maximum of the velocities $u(y)$.

At longer times, the full equation (14) must be used. Then, the value: $R_\infty \simeq (1 + \chi)R(0)$ of the resistance corresponding to a full saturation by the displacing fluid is reached for $t_2^* = U/u_m \geq 1$ (u_m is the minimum velocity).

The result of the computation for $n = 0.26$ is plotted in Fig. 5 as a solid line. The predicted variation corresponds well to the experiments, particularly for $Pe = 285$: in this case, the experimental and theoretical curves coincide precisely in both the linear and in the “tail” parts of the curves.

At lower Péclet numbers, the absolute value of the slope becomes lower: this may be due to the transverse diffusion of fluid between the fastest flow paths and the slower ones.

Replacing the power law fluid by a Newtonian one (dashed line in Fig. 5) strongly reduces the tail effect: the linear variation is retained during a longer time t^* than for the shear thinning solution. This reflects the lower value of the velocity contrasts between the fast and slow paths for the Newtonian solution ($n = 1$) than for $n = 0.26$. The slope of the linear variation is however the same. The reduced value of the experimental slope at lower Pe 's is therefore not accounted for by the vicinity of a Newtonian plateau of the rheological curve at lower shear rates.

Numerical 2D computation of the resistance. In the above model, transverse electrical transport in the y direction is neglected. It will however be present since the aperture field $a(x, y)$ is bidimensional even though it is strongly anisotropic.

In order to estimate its influence, numerical simulations have been performed: the full 2D aperture field $a(x, y)$ is used for computing the electrical resistance while, at all times, the front $x_f(y, t)$ is computed in the same way as above. The fractured is modelled as a two dimensional array of resistors with mesh sizes δl and δw respectively along x and y . The resistance of a node of coordinates (x, y) is taken equal to:

$$r(x, y) = \frac{\delta l}{\sigma a(x, y) \delta w} \quad (17)$$

in which σ is equal to σ_s or σ_d depending on the fluid saturating the node.

The array is considered as a set of bonds linking two nodes of the array and with a resistance equal to the mean of that of the nodes. At each time step, the computation of the equivalent resistance by writing Ohm's law for every bond leads to a set of linear equations solved by means of a conjugate gradient method. Like for the analytical model, the predicted variation of $R^*(t^*)$ with t^* is independent of Pe (local dispersion and molecular diffusion are again neglected).

The variation $R^*(t^*)$ obtained in this way is represented by a dashed-dotted line in Fig. 5. The values obtained are very similar to the predictions of the simpler analytical model (dashed dotted line). This shows that the transverse electrical currents have almost no influence on the electrical resistance, at least in the channel geometry. This justifies therefore the use of the analytical model in the inversion tests discussed below.

4.3. Barrier geometry

Velocity field and front displacement. In this geometry, corresponding to the aperture field of Fig. 2, we assume that the front between the two fluids remains flat at all times; however, its velocity $dx_f/dt = u(x)$ varies with distance so that the flow rate $Q = u(x)a(x)w$ remains constant while the mean aperture $a(x)$ varies (see Fig. 8b). The

transit time $t(x_f)$ of the front from $x = 0$ to $x = x_f$ is:

$$t = \int_0^{x_f} \frac{dx}{u(x)} = \frac{w}{Q} \int_0^{x_f} a(x) dx \quad (18)$$

In contrast with the channel case, this relation does not depend on the rheology of the fluid (the latter influences only the local velocity profile between the walls of the fracture and is therefore not relevant in the present model).

Analytical and numerical computation of the resistance. In this barrier geometry, the global effective resistance is obtained by summing the resistances of the slices corresponding to different distance x and which are, this time, in series. In the case in which solution s is replaced by solution d , this leads to:

$$R(t) = \frac{1}{\sigma_s w} \left(\int_0^L \frac{dx}{a(x)} + \chi \int_0^{x_f(t)} \frac{dx}{a(x)} \right). \quad (19)$$

The slope dR/dt of the variation is not constant with time like in the case of the parallel plates but is given by:

$$\frac{dR(t)}{dt} = \frac{\chi}{\sigma_s w} \frac{Q}{a^2(x)}. \quad (20)$$

in which $Q = a(x)w dx_f/dt$ is (as above) the flow rate.

Eq. (19) may be rewritten using the dimensionless variables R^* defined by Eq. (3) and t^* defined by:

$$t^* = \frac{t(x_f)}{t(L)} = \frac{\int_0^{x_f} a(x) dx}{\int_0^L a(x) dx} = \frac{U t}{L} \quad (21)$$

in which which U is the harmonic mean of the velocities $u(x)$ over the distance L . The variation of R^* as a function of t^* is plotted in Fig. 6 as a solid line and does not depend on Pe .

Like for the experimental data (symbols) and unlike for the channel geometry, no tail is observed but the slope varies significantly during the displacement: from Eq. (20), this reflects the variations of the aperture $a(x)$. Quantitatively, the values obtained are closer to data from the experiments corresponding to the two lowest Péclet numbers ($Pe = 28$ and $Pe = 142$) but slightly higher. This may reflect the increase of the longitudinal dispersion at high flow rates.

Like in the channel geometry, the influence of transverse electrical current on the value of the resistance is verified by computing the electrical resistance by means of a $2D$ numerical computation based on the full aperture $a(x, y)$. In contrast, the front is still assumed to be flat and its displacement is computed as above. The numerical procedure for computing the resistance at a given time is the same as for the channel geometry and the result is plotted in Fig. 6 as a dashed-dotted line.

The values are again very similar to those predicted by the simpler analytical model which is therefore always used for computing the electrical resistance in the inversion procedures below. Globally, the results reported here demonstrate that the barrier and channel structures of the aperture field induce very different deviations from the linear variation of the resistance with time corresponding to a parallel plate model. We

demonstrate now that the resistance measurement may be used to obtain quantitative information on the fracture heterogeneity (this represents indeed a key issue in view of practical applications).

5. Inversion of experimental resistance variation data

Two different approaches are used in this part depending on the occurrence of tailing or of variations of the slope in the plots of the resistance as a function of time.

Practically we seek to determine from the variation of the resistance with time the parameters of the simplified theoretical description from Secs. 4.2 or 4.3 suitable in the case considered.

5.1. Inversion of the data for the channel geometry

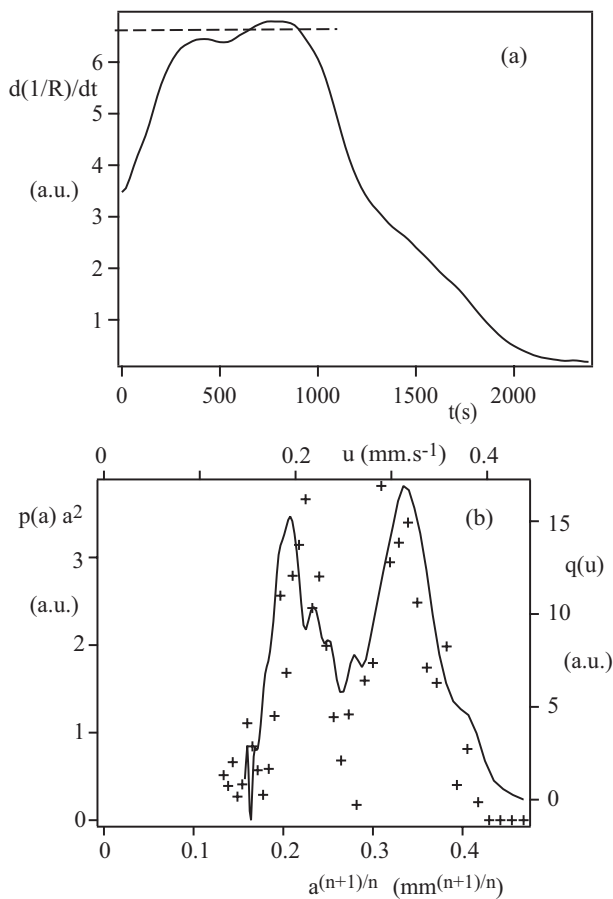


Figure 9: a) Variation of the derivative $d/dt(1/R)$ as a function of time for the experiment at $Pe = 285$ in the channel geometry. b) Compared variations of the distribution $q(u)$ of the flow rate as a function of the velocity u for the same experiment (solid line) and of $a^2 p(a)$ as a function of $a^{(n+1)/n}$ (crosses).

In this case, the resistance variation curves display a roughly linear part and a tail one. Most of the information on the distribution of the apertures and flow velocities is provided by the tail: it corresponds to the transition between the breakthrough of the front at the end of the model ($x = L$) in the fastest channels and in the slowest ones. This is clearly seen by differentiating Eq. (14) with respect to time. Only the first integral contributes to the derivative since the second corresponds to channels already fully saturated with the displacing fluid. This leads to:

$$\frac{d}{dt} \left(\frac{1}{R(t)} \right) = -\frac{\sigma_s \chi}{L^2} \int_{u(y) \leq L} a(y) u(y) dy. \quad (22)$$

The variation of $d(1/R)/dt$ with time is plotted in Fig. 9a. The Péclet number $Pe = 285$ has been selected because it corresponds to the best fit of the theoretical models with the experimental variation. After a transient initial rising part, a plateau value is reached (dashed line) and, then, the slope decreases in the tail part of the curve $R(t)$ (here for $t \geq 800$ s): in the following, this will be the range of times of interest. The initial rise likely corresponds to the time required for the homogeneization of the distribution of the fluids over the distance between the fracture walls after the initial injection.

Actually, the integral in Eq. (22) represents the cumulative flow rate $Q(u_c) = \int_0^{u_c} q(u) du$ in the channels of velocity $u(y) \leq u_c = L/t$: at short times, this condition is met for all channels and $Q(u) = Q$. The derivative $q(u) = dQ/du$ characterizes therefore the distribution of the flow in the model between the channels of different velocities. Derivating Eq. (22) with respect to time leads to:

$$\frac{d^2}{dt^2} \left(\frac{1}{R(t)} \right) = -\frac{\sigma_s \chi}{L^2} \frac{du}{dt} q(u). \quad (23)$$

with $u = L/t$ so that, replacing du/dt as a function of t ,

$$t^2 \frac{d^2}{dt^2} \left(\frac{1}{R(t)} \right) = \frac{\sigma_s \chi}{L} q(u). \quad (24)$$

The distribution $q(u)$ for values of u such that the corresponding time L/u is in the tail region is displayed in Fig. 9b.

The function $q(u)$ may also be related to the normalized probability distribution $p(a)$ of the apertures of the channels. This distribution $p(a)$ has been determined from the mean aperture profile $a(y)$ (see Fig. 1). The function $q(a)$ is then given by $q(a) = w a u(a) p(a)$ and related to $q(u)$ by $q(u) = q(a) da/du$. Also, from Eq. (11), the velocity $u(a)$ in a region of local aperture a is proportional to $a^{(n+1)/n}$. Combining these relations leads to $q(u) \propto a(u)^2 p(a(u))$ (the order of magnitude of the proportionality coefficient may be roughly estimated but its precise value depends on the geometry of the rough surfaces). These two estimations of $q(u)$ are compared in Fig. 9; the scales have been adjusted and the variable $a^{(n+1)/n}$ is used for the horizontal (upper) axis in order to make the comparison easier.

Both distributions have a double peaked shape and the values of ratio between the values of u corresponding to these peaks are also similar. This confirms that information on the flow probability distributions can be obtained from the resistance variation

curves. Obtaining information on the spatial distribution of the flow (particularly in the direction y) is however of course not possible for such global measurements averaged over the width w . Local sensors with some spatial resolution in the direction y would be useful for that purpose.

5.2. Inversion of the data for the barrier geometry

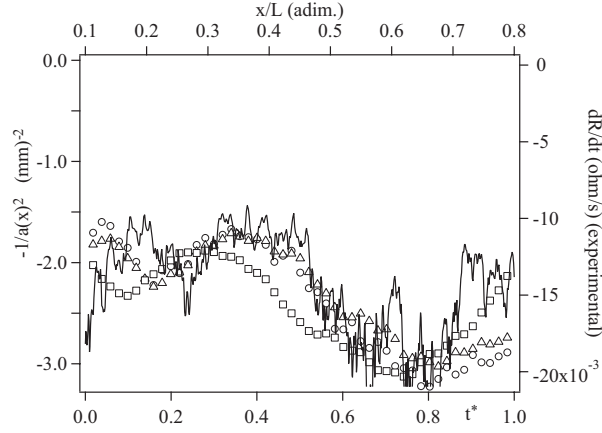


Figure 10: Barrier geometry: compared variations of the experimental time derivative dR^*/dt^* of the resistance for 3 Péclet numbers and of the inverse of the squared aperture $1/a(x)^2$ (continuous line) as a function of the reduced time $t^* = Ut/L$ and of the distance x/L respectively. The values of the experimental parameters and the symbols used for the experimental data are the same as in Fig. 6 and the vertical scales have been selected to make comparisons easier.

In this configuration in which heterogeneities are barriers perpendicular to the mean flow, the variations of the resistance with time allow one to determine the variations of the aperture with distance. Assuming that the aperture has a value $a(x)$ independent of the transverse distance y , Eq. (20) predicts indeed that $dR^*(t^*)/dt^* \propto 1/a(x)^2$. This relation is applicable if local dispersion is negligible: practically, the width of the front must remain small compared to the characteristic distances of variation of the aperture along x .

The validity of Eq. (20) is tested in Fig. 5.2: the variations of $dR^*(t^*)/dt^*$ and $1/a(x)^2$ respectively as a function of the normalized variables t^* and x/L are compared (using these two different horizontal scales amounts to neglect the small deviations of the front velocity from a constant value). One observes an excellent correlation between the large and medium scale variations of both quantities, particularly at the two lowest Péclet numbers.

More globally, we also compared the mean slopes of the variations of $R^*(t^*)$ in the first and second half of the displacement ($0 \leq t^* \leq 0.5$ and $0.5 \leq t^* \leq 1$) to the square a_2^2/a_1^2 of the ratio of the mean apertures in the corresponding regions of the model ($0 \leq x \leq L/2$ and $L/2 \leq x \leq L$). The aperture map of Fig. 2 leads to $a_1 \simeq 0.83$ mm and $a_2 \simeq 0.66$ mm so that $a_2^2/a_1^2 \simeq 0.68$ while the ratio of the slopes of the resistance curve has a comparable value of the order of 0.75.

These results show that, in the “barrier” configuration, quantitative information on the variation $a(x)$ of the mean aperture is readily obtained from the variation of the resistance with time through a simple derivation.

6. Discussion and conclusions

The experimental results reported here demonstrate that measurements of the variation with time of the global electrical resistance during a miscible displacement experiment provides quantitative information on the large and medium scale variations of the local velocity and aperture in rough fractures.

We have found that, in order to make the interpretation simpler, the contrast between the electrical conductivities of the two fluids must be moderate. Practically, information is provided by the deviation of the variation of the resistance from that for a parallel plate system of same effective aperture. It has also been verified that using shear thinning fluids enhances the velocity contrasts between the different flow paths and may help detecting the heterogeneities.

Preferential channels parallel to the mean flow (channel geometry) lead to deviations from the parallel plate variation due to early breakthrough at the outlet of the fracture; slow channels delay instead the full saturation of the medium. The velocity contrasts between these different channels as well as the distribution of the aperture may be estimated from the values of these early and late arrival times.

Barrier type features extending over a large fraction (or all) the fracture width induce deviations of the derivative dR/dt of the variation of the resistance with time from its average value: the variations of this derivative were shown to vary as the inverse of the square of the local aperture (at least for large and medium scale variations).

Local dispersion and/or heterogeneities also influence the variation of the resistance, particularly when the front width is not negligible compared to the length of the sample. Deviations associated to the longitudinal dispersion take then place mostly when the displacement front leaves the fracture. Transverse dispersion is also observed to influence the resistance: it reduces for instance the derivative of its variation with respect to time: such effects may be used to characterize this process.

The measurements described in the present paper are applicable to natural fractured rocks like those encountered in the granitic field sites used previously for hydromechanical experiments (Cornet et al., 2003). In such cases the surface conductivity of the rocks (due for instance to clay minerals) often needs to be taken into account (Ruffet et al., 1995): the analysis of the frequency dependence of the real and imaginary parts of the impedance may then provide useful complementary information. In the case of fractured porous rocks, retardation effects due to solute exchange between the pores and the fracture must also be taken in consideration. Finally additional information may be obtained by using several local electrodes at the inlet and outlet of the sample in order to achieve some lateral resolution in the direction transverse to the flow.

Acknowledgments

We are indebted to A. Aubertin and R. Pidoux for their assistance. H. A. and J. P. H. are supported by CNRS through GdR 2990 and by the European Hot Dry Rock Associ-

ation. This work was greatly facilitated by the CNRS-Conicet International Associated Laboratory LIA-PMF (Physics and Mechanics of Fluids) and the cooperation agreement n° 22815, the “Triangle de la Physique” RTRA Program and by the UBACYT I044 program.

Auradou, H., Drazer G., Hulin J.P. et Koplik J. (2005) Permeability anisotropy induced by the shear displacement of rough fracture walls, *Water Resources Research*, **41**, W09423.

Bauget, F., M. Fourar (2008), Non-Fickian dispersion in a single fracture. *J. Cont. Hydro.* **100**, 137148.

Boschan, A., J. Charette, S. Gabbanelli, I. Ippolito, R. Chertcoff (2003), Tracer dispersion of non-newtonian fluids in a Hele Shaw cell. *Physica A*, **327**, 49-53.

Boschan, A., H. Auradou, I. Ippolito, R. Chertcoff, and J. P. Hulin (2009), Experimental evidence of the anisotropy of tracer dispersion in rough fractures with sheared walls, *Water Resour. Res.*, **45**, W03201.

Bouchaud, E. (2003), The morphology of fracture surfaces: A tool for understanding crack propagation in complex materials, *Surf. Rev. Lett.*, **10**, 797–814.

Brown, S. R. (1989), Transport of fluid and electric current through a single fracture, *J. Geophys. Res.* **94**, 9429–9438.

Cornet, F.H., L. Li, J.-P. Hulin, I. Ippolito and P. Kurowski (2003), The hydromechanical behaviour of a fracture: an in situ experimental case study, *Int. J. Rock Mech. and Min. Sci.*, **40**, 12571270.

Horobin, R.W. and J.A Kiernan (Eds) (2002), *Conn’s Biological Stains: A Handbook of Dyes, Stains and Fluorochromes for Use in Biology and Medicine*, BIOS Scientific Publishers Ltd.

Keller, A. A., P. V. Roberts, and M. J. Blunt (1999), Effect of Fracture Aperture Variations on the Dispersion of Contaminants, *Water Resour. Res.*, **35**, 55–63.

Matsuki K., Chida Y., Sakaguchi K. and Glover P.W.J. (2006), Size effect on aperture and permeability of a fracture as estimated in large synthetic fractures , *Int. J. Rock Mech. Min. Sci.***43** 72655.

Y. Méheust and J. Schmittbuhl (2000), Flow enhancement of a rough fracture, *Geophys. Res. Lett.* **27**, 2989.

NAS Committee on Fracture Characterization and Fluid Flow, *Rock Fractures and Fluid Flow: Contemporary Understanding and Applications* (National Academy Press, Washington, D.C., 1996).

Nemoto K., Watanabe N., Hirano N. and Tsuchiya N. (2009), Direct measurement of contact area and stress dependence of anisotropic flow through rock fracture with heterogeneous aperture distribution, *Earth Planet. Sci. Lett.***281** 817

- I. Neretnieks, T. Erksen and P. Tahtinen (1982), Tracer movement in a single fissure in granitic rock: some experimental results and their interpretation. *Water Resour. Res.* **18**, 849.
- Neretnieks, I. 2002. A stochastic multi-channel model for solute transport. Analysis of tracer tests in fractured rock. *Water Resour. Res.* **55**, 175–211.
- Odling, N.W.A, S.C. Elphick, P. Meredith, I. Main and B.T. Ngwenya (2007), Laboratory measurements of hydrodynamic saline dispersion within a micro-fracture network induced in a granite, *Earth Planet. Sci. Lett.* **260**, 407-418.
- Oron, A. P., and B. Berkowitz (1998), Flow in Rock Fractures: The Local Cubic Law Assumption Reexamined, *Water Resour. Res.*, **34**, 2811–2825.
- Plouraboué, F., P. Kurowski, J-M. Boffa, J-P. Hulin and S. Roux (2000), Experimental study of the transport properties of rough self-affine fractures, *J. Cont. Hydro.* **46**, 295318.
- Poon, C., R. Sayles, and T. Jones (1992), Surface measurement and fractal characterization of naturally fractured rocks, *J. Phys. D Appl. Phys.*, **25**, 1269–1275.
- Ruffet, C., M. Darot, and Y. Gueguen (1995), Surface Conductivity In Rocks - A Review, *Surv. Geophys.*, **16**, 83-105.
- Taylor, G. I. (1953) Dispersion of soluble matter in solvent flowing slowly through a tube , *Proc. Roy. Soc. A.*, **219**, 186–203.
- Watanabe N., Hirano N., and Tsuchiya N.(2008) Determination of aperture structure and fluid flow in a rock fracture by high-resolution numerical modeling on the basis of a flow-through experiment under confining pressure , *Water Resour. Res.*,**44** W06412.
- Yeo I. W., M. H. De Freitas, and R. W. Zimmerman (1998), Effect of shear displacement on the aperture and permeability of a rock fracture, *Int. J. Rock Mech. and Min. Sci.*, **35**, 1051–1070.